Antiferromagnetic interlayer exchange coupling and large spin Hall effect in multilayer systems with Pt/Ir/Pt and Pt/Ir layers

Yoshiaki Saito [1,*] Nobuki Tezuka,[2,3] Shoji Ikeda,[1,3,4,5] and Tetsuo Endoh[1,3,4,5,6]

[1]*Center for Innovative Integrated Electronic Systems, Tohoku University, Sendai 980-0845, Japan*
[2]*Department of Materials Science, Graduate School of Engineering, Tohoku University, Sendai 980-8579, Japan*
[3]*Center for Spintronics Research Network, Tohoku University, Sendai 980-8577, Japan*
[4]*Center for Science and Innovation in Spintronics, Tohoku University, Sendai 980-8577, Japan*
[5]*Research Institute of Electrical Communication, Tohoku University, Sendai 980-8577, Japan*
[6]*Department of Electrical Engineering, Graduate School of Engineering, Tohoku University, Sendai 980-8579, Japan*

We investigated Pt/Ir/Pt and Pt/Ir multilayers as candidates of nonmagnetic spacer layers in synthetic antiferromagnetic (AF) layers, which are available for the systematic study on AF spintronics. In these systems, we observed (i) AF interlayer exchange coupling in Pt/Ir/Pt and Pt/Ir nonmagnetic spacer layers sandwiched by Co layers and (ii) large spin Hall conductivity in Pt/Ir multilayer heavy-metal systems which is essential to achieve low power consumption spin-orbit torque switching. We found that total nonmagnetic spacer layer thickness $[t_{\text{total}} = t_{\text{Pt}}(\text{Pt thickness}) + t_{\text{Ir}}(\text{Ir thickness})]$ range in which AF interlayer exchange coupling is observed is wide in Co/nonmagnetic spacer layer/Co with Pt/Ir/Pt and Pt/Ir nonmagnetic spacer layers. Moreover, the large spin Hall angle of $\theta_{\text{SH}} = 10.3\%$ and low resistivity of $\rho_{xx} = 35\,\mu\Omega\,\text{cm}$ in Pt/Ir multilayer heavy metal are observed. These results indicate that Pt/Ir/Pt and Pt/Ir are nonmagnetic spacer layers allowing us to achieve the AF interlayer exchange coupling and generation of large spin-orbit torque via spin Hall effect in synthetic AF coupling layer system.

I. INTRODUCTION

Antiferromagnetic (AF) materials [1–16] have attracted attention due to their fast magnetization dynamics using current-induced spin-orbit torque (SOT) originating from the spin Hall effect (SHE) [17–34], low magnetic susceptibility, and lack of magnetic stray field. Up to now, several works reported the manipulation of AF structures using electric current [3,7–16]. The manipulation of AF structures in CuMnAs, which is one of the bulk AF materials, was demonstrated using current-induced internal fields originating from its crystal structure with broken inversion symmetry [7]. Nickel oxide (NiO) is also a bulk AF material, and its antiferromagnetically coupled magnetic moments (Néel vector) could be switched by SOT originating from SHE by using the two Pt layers adjacent to the outside of the NiO layer [8]. Thus, most studies of AF spintronics have focused on bulk AF materials. For the bulk AF materials, the complicated AF domain structures are often observed [10,14,15], and intrinsic AF-coupling strength is uncontrollable.

On the other hand, a metallic superlattice having an AF structure, in which the ferromagnetic layers separated by the nonmagnetic spacer layer are antiferromagnetically coupled through interlayer exchange coupling (synthetic AF coupling layer) [35,36], was proposed as another candidate system for studying AF spintronics using current-induced SOT switching originating from the SHE [16,37]. Because nonmagnetic spacer layers such as Ru, Cu, and Ir, which are representative materials of nonmagnetic spacer layers in the synthetic AF coupling layer, have small SHE (spin Hall angle: $\theta_{\text{SH}} \sim 0.6\%$, $\sim 0.3\%$, and $\sim 2\%$, respectively) [38–40], Dai *et al.* proposed the use of two Pt layers adjacent to the outside of the synthetic AF coupling layer and utilization of the relatively large SHE of the two adjacent Pt layers ($\theta_{\text{SH}} \sim 6$–10%) [33,39,41–43] in Pt/Co/Ru/Co/Pt multilayers [37]. Masuda *et al.* proposed the material of Ir-doped Cu alloy (Cu-Ir) for nonmagnetic spacer layer in the synthetic AF coupling layer of Co/Cu-Ir/Co and observed the AF coupling through $Cu_{95}Ir_5$ alloy with a relatively large SHE ($\theta_{\text{SH}} = 3$–4%) in the thickness (t_{CuIr}) range of $0.6 < t_{\text{CuIr}} < 1.0$ [16]. However, in the case of the idea of Ref. [37], considering an application of SOT-magnetic random-access memory (MRAM) shown in Fig. 1(a), the Pt layer insertion between synthetic AF coupling layer and a read device such as magnetic tunnel junction (MTJ) is not preferable to control the magnetization direction of storage layer in the read device by utilizing the exchange interaction between the storage and the synthetic AF coupling layer. On the other hand, the idea and the findings of Ref. [16] have advantages in terms of the magnetization direction control of the storage layer; however, resistivity (ρ_{xx}) of $Cu_{95}Ir_5$ alloy is relatively large (92.42 $\mu\Omega$ cm) [16]. In the case of the memory cell we proposed in Figs. 1(a) and 1(b), the spacer layer should have large $|\theta_{\text{SH}}|$, low ρ_{xx}, and a thickness sufficiently thicker than the spin-diffusion length, because we would like to pass most of the current through the spacer
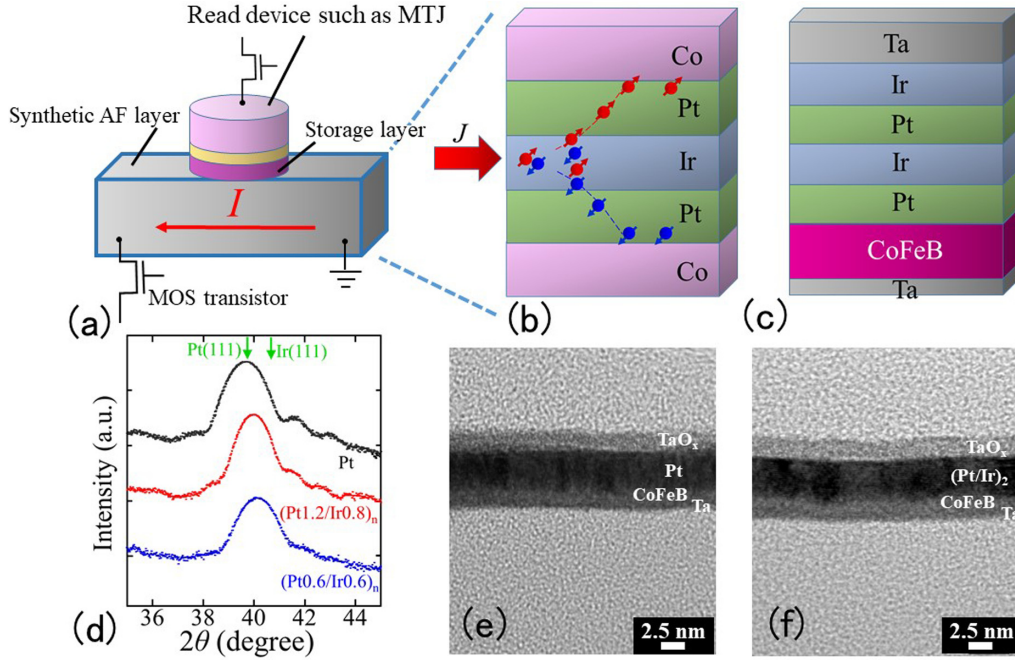
*ysaito@cies.tohoku.ac.jp

FIG. 1. (a) Schematic diagram for memory cell of spin-orbit torque (SOT)-MRAM with metal-oxide-semiconductor (MOS) transistors and synthetic antiferromagnetic (AF) layer. The red arrow shows the current (I) direction. (b) Proposed synthetic AF coupling layer structure with Pt/Ir/Pt nonmagnetic spacer layer. (c) An example of sputtered film stacks for measurement of SHE and resistivity of Pt/Ir multilayer HM. (d) Out-of-plane XRD profiles for the stacks with Pt 7 nm (sample E), [Pt(1.2)/Ir(0.8)]$_4$ (sample J), and [Pt(0.6)/Ir(0.6)]$_6$ (sample K) multilayer HMs on Ta (0.5)/CoFeB (1.5) layers. Cross-sectional transmission electron microscopy images in (e) Ta(0.5)/CoFeB(1.5)/Pt(3.5)/Ta(1) and (f) Ta(0.5)/CoFeB(1.5)/[Pt(1.0)/Ir(0.8)]$_2$/Ta(1). The top Ta layers are completely oxidized.

layer in synthetic AF coupling layer. Therefore, if one can find a nonmagnetic spacer layer simultaneously exhibiting AF interlayer exchange coupling and having large $|\theta_{SH}|$, low ρ_{xx} and the thickness sufficiently thicker than the spin-diffusion length, synthetic AF coupling layer is one of the promising systems for the systematic investigation of the SOT on the AF structure.

Here, we try to study the multilayer systems for the investigation of the heavy-metal (HM) material, because we found the large SHE and low ρ_{xx} in [W/Hf]-multilayer HM compared to those in β-phase W [34,44]. This result suggests that artificially synthesized multilayer system is one of the avenues for realizing large $|\theta_{SH}|$ and low ρ_{xx}. Considering the four facts that (i) MTJs with perpendicular magnetic anisotropy (perpendicular MTJs) are the mainstream in current MRAM, (ii) compatibility with crystal growth, (iii) independence of damping factor on the magnitude of switching current in the SOT-MRAM with perpendicular MTJs, and (iv) large SHE in Pt and W [17,20,22,26,28,32–34], Pt/Co and W/CoFeB-related systems would be two of the promising candidates for the application to the large-scale integration (LSI). As the candidate of Pt/Co-related system, we chose the material of the [Pt/Ir]-multilayer HM.

This study focuses on the Pt/Ir/Pt and Pt/Ir nonmagnetic spacer layers sandwiched by Co ferromagnetic layers and investigates the interlayer exchange coupling through Pt/Ir/Pt and Pt/Ir nonmagnetic spacer layers and the magnitude of $|\theta_{SH}|$, σ_{SH}, and ρ_{xx} in [Pt/Ir]-multilayer HM, where σ_{SH} is spin Hall conductivity. We chose to study the Pt/Ir/Pt and Pt/Ir nonmagnetic spacer layers, because Co/Ir/Co is well known

to have a strong AF interlayer exchange coupling [45] and the combination of Pt and Ir is insoluble and same face-centered-cubic (fcc) structure. The same structure of Ir and Pt suggests that topological characteristic of the Fermi surface of Ir and Pt are nearly the same, which would be closely related to the spanning wave vectors (q_s) linking two points of Fermi surface with antiparallel velocities in the case of noble-metal spacer, considering the extended Ruderman-Kittel-Kasuya-Yosida (RKKY) exchange model [46,47]. Therefore, we thought that the Co/Pt/Ir/Pt/Co synthetic AF coupling layer structure shown in Fig. 1(b) might be a candidate simultaneously exhibiting AF interlayer exchange coupling and large SHE.

II. EXPERIMENTAL PROCEDURE

We prepared many samples with various film stacks by rf magnetron sputtering on oxidized Si substrates. Base pressure of the sputtering system is less than 1×10^{-6} Pa. Details of sample structure (stack) are shown in Table I. In order to confirm the magnetic and interlayer exchange coupling properties, we prepared Ta(3)/Pt(3)/[Co(0.9)/Ir(t_{Ir})/Pt(0.6)]$_3$/Co(0.9)/Ir(1)/Ta(2) (sample A) films, Ta(3)/Pt(3)/[Co(0.5)/Pt(0.26)]$_4$/Co(0.5)/Ir(t_{Ir})/Co(0.5)/[Pt(0.26)/Co(0.5)]$_4$/Pt(3) films (sample B) with various t_{Ir}, Ta(3)/Pt(3)/[Co(t_{Co})/Ir(t_{Ir})/Pt(t_{Pt})]$_n$/Co(t_{Co})/Ir(1)/Ta(2) (sample C), and Ta(3)/Pt(3)/[Co(t_{Co})/Pt(t_{Pt})/Ir(t_{Ir})/Pt(t_{Pt})]$_n$/Co(t_{Co})/Ir(1)/Ta(2) (sample D) (n: repetition number) [Fig. 1(b) shows the case of $n = 1$], where numbers in the parentheses show the nominal thickness in nm.

TABLE I. Sample structure (stack) prepared in this study.

Sample name	Structure of prepared films	t_{Ir} (nm)		
A	Ta(3)/Pt(3)/[Co(0.9)/Ir(t_{Ir})/Pt(0.6)]$_2$/Co(0.9)/Ir(1)/Ta(2)	0.4, 0.5, 0.6, 0.7, 0.8, 0.9, 1.0, 1.1, 1.2, 1.3, 1.4, 1.5, 1.6		
B	Ta(3)/Pt(3)/[Co(0.5)/Pt(0.26)]$_4$/Co(0.5)/Ir(t_{Ir})/Co(0.5)/[Pt(0.26)/Co(0.5)]$_4$/Pt(3)	0.4, 0.5, 0.6, 0.7, 0.8, 0.9, 1.0, 1.1, 1.2, 1.3, 1.4, 1.5, 1.6		

Sample name	Structure of prepared films	t_{Co} (nm)	t_{Pt} (nm)	t_{Ir} (nm)	t_{total} (nm)
C	Ta(3)/Pt(3)/[Co(t_{Co})/Ir(t_{Ir})/Pt(t_{Pt})]$_n$/Co(t_{Co})/Ir(1)/Ta(2) ($n = 1$ and $n = 2$)	1.3	0.6, 1.0	0.5, 0.55, 0.6, 1.4, 1.5	1.1, 1.15, 1.5, 1.6, 2, 2,1
D	Ta(3)/Pt(3)/[Co(t_{Co})/Pt(t_{Pt})/Ir(t_{Ir})/Pt(t_{Pt})]$_n$/Co(t_{Co})/Ir(1)/Ta(2) ($n = 1$ and $n = 2$)	1.1, 1.3	0.6, 0.8, 1.0	0.5	1.6, 1.7, 2.1, 2.5

Sample name	Structure of prepared films	Repetition number	$t_{total} = t_{Pt} + t_{Ir}$ (nm)
E	Ta(0.5)/CoFeB(1.5)/Pt(t_{Pt})/Ta(1)	-	1.5, 2.0, 2.5, 3.0, 3.5, 4.0, 4.5, 5.0, 7.0
F	Ta(0.5)/CoFeB(1.5)/[Pt(0.4)/Ir(0.4)]$_n$ multilayer/Ta(1)	$n = 1 \sim 8$	1.6, 2.4, 3.2, 4.0, 4.8, 5.6, 6.4, 7.2
G	Ta(0.5)/CoFeB(1.5)/[Pt(0.6)/Ir(0.6)]$_n$ multilayer/Ta(1)	$n = 1 \sim 6$	1.2, 2.4, 3.6, 4.8, 6.0, 7.2
H	Ta(0.5)/CoFeB(1.5)/[Pt(0.8)/Ir(0.8)]$_n$ multilayer/Ta(1)	$n = 1 \sim 5$	1.6, 3.2, 4.8, 6.4, 8.0
I	Ta(0.5)/CoFeB(1.5)/[Pt(1.0)/Ir(0.8)]$_n$ multilayer/Ta(1)	$n = 1 \sim 5$	1.8, 3.6, 5.4, 7.2, 9.0
J	Ta(0.5)/CoFeB(1.5)/[Pt(1.2)/Ir(0.8)]$_n$ multilayer/Ta(1)	$n = 1 \sim 5$	2.0, 4.0, 6.0, 8.0, 10.0
K	Ta(0.5)/CoFeB(1.5)/[Pt(0.6)/Ir(0.6)]$_n$ multilayer/Ta(1)	$n = 1 \sim 6$	1.2, 2.4, 3.6, 4.8, 6.0, 7.2
L	Ta(0.5)/CoFeB(1.5)/[Pt(0.8)/Ir(0.6)]$_n$ multilayer/Ta(1)	$n = 1 \sim 5$	1.4, 2.8, 4.2, 5.6, 7.0, 8.4
M	Ta(0.5)/CoFeB(1.5)/[Pt(1.0)/Ir(0.6)]$_n$ multilayer/Ta(1)	$n = 1 \sim 5$	1.6, 3.2, 4.8, 6.4, 8.0
N	Ta(0.5)/CoFeB(1.5)/[Pt(1.2)/Ir(0.6)]$_n$ multilayer/Ta(1)	$n = 1 \sim 5$	1.8, 3.6, 5.4, 7.2, 9.0

The films of Ta(0.5)/CoFeB(1.5)/Pt(t_{Pt})/Ta(1) (sample E) and Ta(0.5)/CoFeB(1.5)/[Pt(t_{Pt})/Ir(t_{Ir})]$_n$ multilayer (t_{total})/Ta(1) (samples F–N) systems shown in Figs. 1(c), 1(e), and 1(f) with various Co, Ir, Pt, and total thickness of the HM (t_{Co}, t_{Ir}, t_{Pt}, t_{total}, respectively) are also prepared for measurement of electrical properties. Samples E–N with various t_{Ir}, t_{Pt}, and t_{total} were patterned into the microscale Hall bar by photolithography and Ar ion milling. Detailed fabrication process was described elsewhere [32]. All films and the processed devices were then annealed at 573 K in vacuum less than 1×10^{-4} Pa for 1 h.

Magnetic properties were measured using a vibrating sample magnetometer (VSM) at room temperature. Structural characterization was carried out using cross-sectional high-resolution transmission electron microscopy (HR-TEM) and out-of-plane x-ray diffraction (XRD) with Cu-Kα radiation at room temperature. The transport properties were characterized using four terminal configurations in a physical property measurement system (PPMS, Quantum Design). The prepared devices with various t_{total} were used for measuring ρ_{xx} and SHE by spin Hall magnetoresistance (SMR) method at 305 K. For the measurements of SMR, the current, which is less than equal to 5 μA, is passed through the devices and external magnetic field between -4 and $+4$ T is applied to the devices.

III. RESULTS AND DISCUSSION

A. Structural feature of (Pt/Ir) multilayer

Figure 1(d) shows the typical results of out-of-plane XRD measurements for samples E ($t_{Pt} = 7$ nm), J ($n = 4$, $t_{total} = 8$ nm) and K ($n = 6$, $t_{total} = 7.2$ nm). The results show that the Pt and [Pt/Ir]$_n$ HMs have a fcc structure with the (111) texture. As shown in Fig. 1(d), the peak 2θ positions of Pt and [Pt/Ir]$_n$ HMs are consistent with peak 2θ position of bulk Pt (111) and that between bulk Pt (111) and bulk Ir (111). The observed satellite peaks in Fig. 1(d) are reminiscent of the designed multilayer structure. However, the satellite peaks

were also observed in Pt monolayer as shown in Fig. 1(d). In addition, assuming the multilayer formation, the artificial thickness period ($\lambda_{multilayer}$) by using the 2θ distance between the XRD main peak and first satellite peak is estimated to be $\lambda_{multilayer} \sim 3$ nm, which is much larger than the designed value of $\lambda_{multilayer} = 1.2 \sim 2.0$ nm. Therefore, the possible reason for observing the satellite peaks in Fig. 1(d) could originate from flat and high-quality Pt and [Pt/Ir]$_n$ multilayer HMs as observed in high-quality semiconductor multilayer system [48].

Figures 1(e) and 1(f) show the cross-sectional HR-TEM results for samples E ($t_{Pt} = 3.5$ nm) and I ($n = 2$, $t_{total} = 3.6$ nm), respectively. Flat and (111)-textured Pt and [Pt/Ir]-multilayer HMs were observed. The averaged grain sizes are ~ 8 and ~ 12 nm for Pt(3.5) and [Pt(1.0)/Ir(0.8)]$_2$, respectively. From the results of the cross-sectional HR-TEM results, there is no noticeable difference in terms of the texture and surface roughness between Pt(3.5) and [Pt(1.0)/Ir(0.8)]$_2$ films. We also found that top Ta layers are completely oxidized as shown in Figs 1(e) and 1(f).

B. Magnetic properties and interlayer exchange coupling

Figures 2(a)–2(c) and Figs. 2(d)–2(f) show the normalized out-of-plane and in-plane magnetization versus field (*M-H*) curves for samples A ($t_{Ir} = 0.5$, 1.0, 1.4) and B ($t_{Ir} = 0.5$, 1.0, 1.4), respectively. The film structures (stacks) of samples A and B are shown in Figs. 2(g) and 2(h), respectively. The arrows in the light-pink color boxes in Figs. 2(a)–2(f) indicate the corresponding magnetization state: top, middle, and bottom arrows in Figs. 2(a)–2(c) represent the magnetization direction of the top, middle, and bottom Co layers, and top and bottom arrows in Figs. 2(d)–2(f) represent the magnetization direction of the top and bottom Co layers. The *M-H* curves in Figs. 2(a), 2(c), 2(d), and 2(f) show AF interlayer exchange coupling between Co layers through Ir/Pt and Ir layers, and those in Figs. 2(b) and 2(e) show ferromagnetic (F)
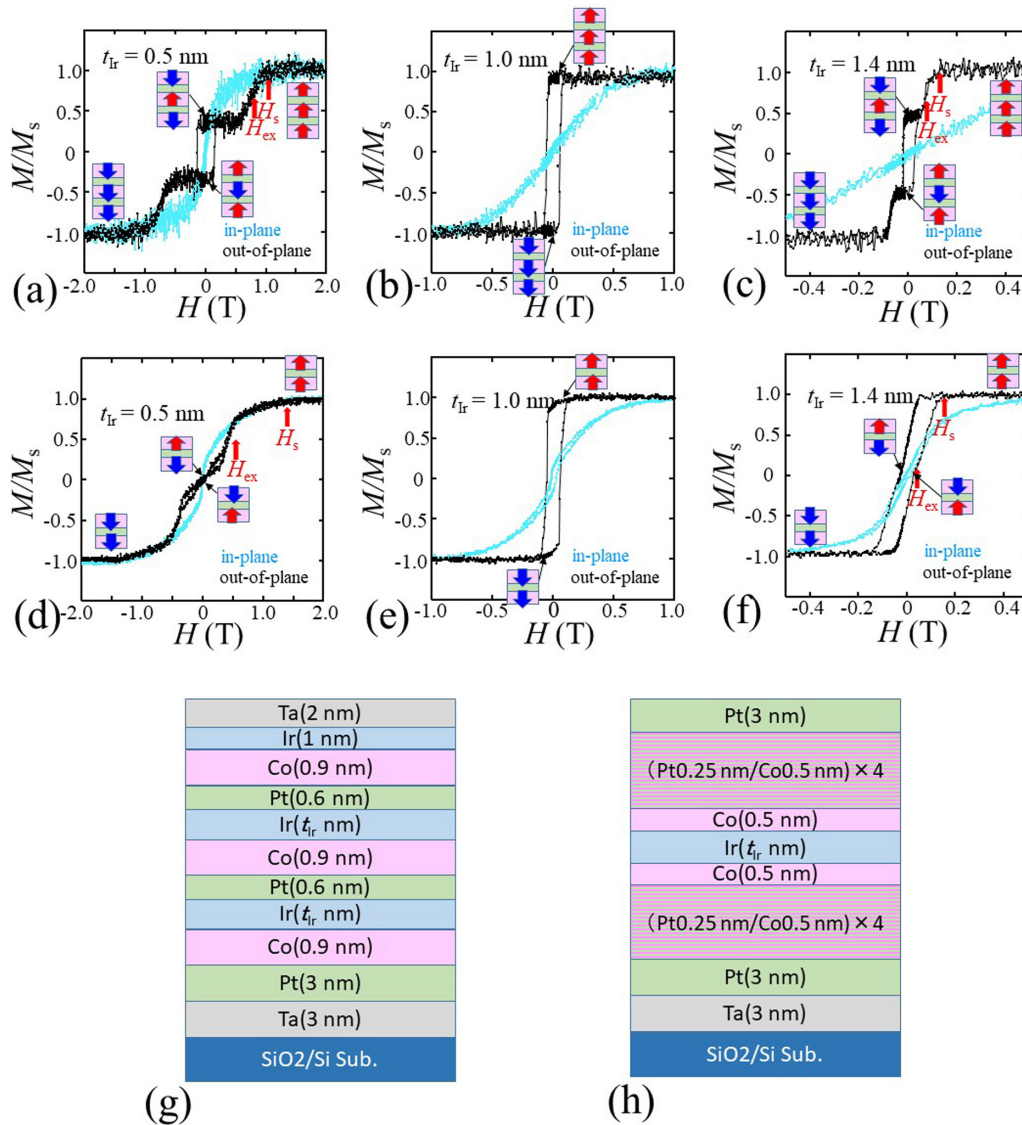
FIG. 2. Normalized magnetization vs field (*M-H*) curves for (a)–(c) sample A (t_{Ir} = 0.5, 1.0, 1.4 nm) and (d)–(f) sample B (t_{Ir} = 0.5, 1.0, 1.4 nm). The red and blue arrows in the light-pink color boxes in (a)–(f) indicate the corresponding magnetization state and the magnetization direction of each Co layer. (g) (h) Film structures (stacks) of samples A and B.

interlayer exchange coupling between Co layers through Ir/Pt and Ir layers. These *M-H* curves are consistent with previous results [45,49]. Thus, we observed the oscillation of interlayer exchange coupling as a function of t_{Ir}. Figure 3 shows the plot of magnitude of the interlayer exchange coupling ($|J_{ex}|$) as a function of t_{Ir} for samples A and B. The magnitude of $|J_{ex}|$ was evaluated using $|J_{ex}| = M_s t H_{ex}$ [50,51], where M_s, *t*, and H_{ex} are the saturation magnetization of Co, thickness of the Co/Pt layers, and the exchange field (H_{ex}) defined in Figs. 2(a), 2(c), 2(d), and 2(f). The values of *t* and M_s for samples A and B are *t* = 1.5 nm, M_s = 0.87 T, and *t* = 3.54 nm, M_s = 1.27 T, respectively. As shown in Fig. 3, we observed first and second peaks of $|J_{ex}|$ as a function of t_{Ir}. Magnitude of $|J_{ex}|$ for sample B (direct interlayer exchange through Ir layer) is consistent with previous report [45] and is larger than the magnitude of $|J_{ex}|$ through Pt/Ir bilayers observed in sample A. The oscillation period of AF interlayer exchange coupling Λ is about 0.95 nm for both samples A and B. According to the

extended RKKY exchange model [46,47], the Λ is given by $\Lambda = 2\pi/q_s$, where q_s is the spanning wave vector linking two points of Fermi surface with antiparallel velocities. Therefore, the same Λ values for samples A and B and no shift in the oscillation observed in Fig. 3 indicate that the sign and intensity of the J_{ex} do not oscillate with increasing t_{Pt}. If this interpretation is correct, we could observe the AF interlayer exchange coupling through Pt/Ir/Pt trilayers in which this structure would be useful for the systematic investigation of the SOT on the AF structure shown in Figs. 1(a) and 1(b), because we utilize large SHE in Pt.

In order to confirm this interpretation, we prepared sample C with various t_{Pt} and t_{Ir} and sample D with various t_{Pt} and t_{Co}. Figures 4(a) and 4(b) show the typical normalized out-of-plane and in-plane *M-H* curves for samples D (*n* = 2, t_{Co} = 1.3 nm, t_{Pt} = 0.8 nm) and D (*n* = 1, t_{Co} = 1.1 nm, t_{Pt} = 0.8 nm), respectively. As shown in Fig. 4(a), for sample D (*n* = 2, t_{Co} = 1.3 nm, t_{Pt} = 0.8 nm), the magnitudes of the
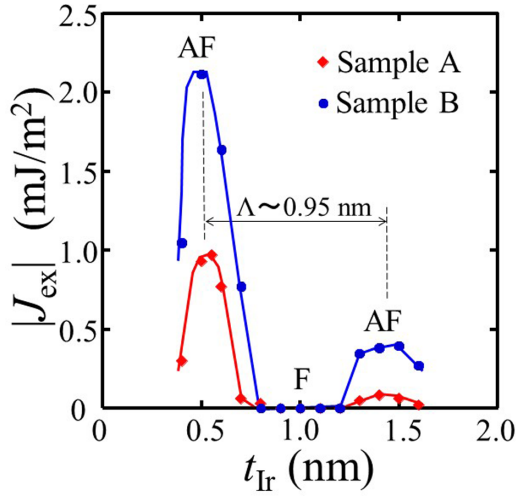
FIG. 3. Magnitude of the interlayer exchange coupling ($|J_{ex}|$) as a function of Ir thickness (t_{Ir}) measured at room temperature in samples A and B. The oscillation period (Λ) of AF interlayer exchange coupling is about 0.95 nm for both films.

remanent magnetization in out-of-plane and in-plane *M-H* curves are almost 1/3 and zero, respectively. For sample D ($n = 1$, $t_{Co} = 1.1$ nm, $t_{Pt} = 0.8$ nm), the magnitudes of the remanent magnetization in out-of-plane and in-plane *M-H*
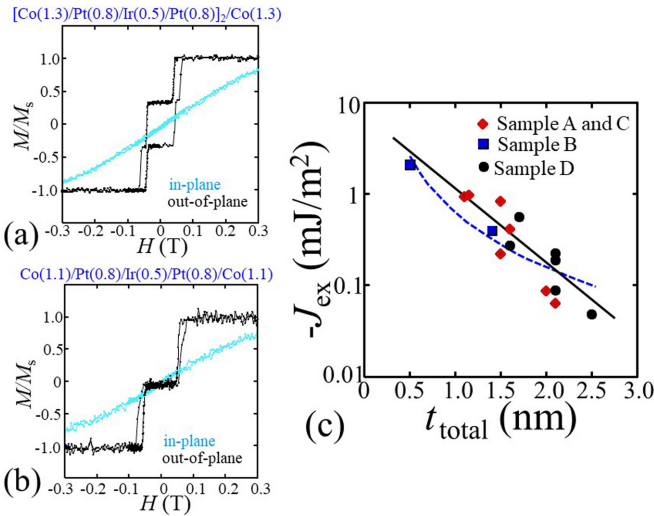

FIG. 4. Normalized *M-H* curves for (a) Ta(3)/Pt(3)/[Co(1.3)/Pt(0.8)/Ir(0.5)/Pt(0.8)]$_2$/Co(1.3)/Ir(1)/Ta(2) [sample D ($n = 2$, $t_{Co} = 1.3$ nm)] and (b) Ta(3)/Pt(3)/Co(1.1)/Pt(0.8)/Ir(0.5)/Pt(0.8)/Co(1.1)/Ir(1)/Ta(2) [sample D ($n = 1$, $t_{Co} = 1.1$ nm)]. AF interlayer exchange coupling through Pt/Ir/Pt trilayers was observed. (c) AF interlayer exchange coupling ($-J_{ex}$) as a function of $t_{total} = t_{Pt} + t_{Ir}$ for sample C with various t_{Pt} and t_{Ir} and sample D with various t_{Pt} and t_{Co}. The $-J_{ex}$ values of first and second peak positions ($t_{Ir} = 0.5$, 1.4 nm) in sample B are also plotted in (c). The black solid line and blue dotted line in (c) are the results of least-square fit using the equation $-J_{ex} \propto \exp(a - b\,t_{total})$, where a and b are fitting parameters ($a = 1.5$, $b = 1.856$), and $-J_{ex} \propto t_{total}^{-2}$. The -2nd power law of the t_{total} is the result of fitting assuming the RKKY interaction [72,73].

curves shown in Fig. 4(b) are almost zero. Thus, we observed the AF interlayer exchange coupling through Pt/Ir/Pt trilayers. Figure 4(c) shows the $-J_{ex}$ as a function of $t_{total} = t_{Pt} + t_{Ir}$ for sample C with various t_{Pt} and t_{Ir} and sample D with various t_{Pt} and t_{Co}. The $-J_{ex}$ values of first and second peak positions ($t_{Ir} = 0.5$, 1.4 nm) in sample B are also plotted in Fig. 4(c). As shown in Fig. 4(c), monotonous decrease in $-J_{ex}$ with increasing t_{total} was observed. Thus, we observed AF interlayer exchange coupling through both Pt/Ir and Pt/Ir/Pt between 1.0 nm $\leqslant t_{total} \leqslant 2.5$ nm. The observation of AF interlayer exchange coupling through a wide thickness range of t_{total} and t_{Pt} (0 nm $\leqslant t_{Pt} \leqslant 1.0$ nm) indicates that the sign of the interlayer exchange coupling does not oscillate in Pt. The observed relatively large magnitude of AF interlayer exchange coupling through relatively thick nonmagnetic spacer of Pt/Ir/Pt would useful for the SOT on the AF structure.

C. Electrical properties

As shown before, we observed relatively large magnitude of AF interlayer exchange coupling through thick nonmagnetic spacer of 1.5 nm $< t_{total} \leqslant 2.5$ nm in Co/Pt/Ir/Pt/Co system. Next, we show the estimated results of electrical properties such as ρ_{xx}, θ_{SH}, and σ_{SH} in [Pt/Ir]-multilayer HM. We evaluate the SHE using the SMR measurement, because we can evaluate ρ_{xx}, θ_{SH}, and σ_{SH} simultaneously and correctly. In a nonmagnetic layer/ferromagnetic layer system, the electrical resistance difference that occurs when the ferromagnetic magnetization direction is changed in a plane orthogonal to the current flow direction is called SMR. The origin of the SMR is related to that a spin absorption of spin current in a nonmagnetic layer generated by the SHE differs depending on the relative angle of the spin directions between the spin current and a ferromagnetic layer. Since it is known [52] that the θ_{SH} can be measured correctly by using a magnetic insulator [53] or a magnetic layer with high resistance such as CoFeB [32–34,52,54,55] for SMR measurement, we decided to use CoFeB instead of Co for the SHE evaluation in [Pt/Ir]-multilayer HM.

Figures 5(a) and 5(b) show the film stacks in prepared Hall bar devices. Figures 5(c) and 5(d) show the schematic diagram of the Hall bar device and an example of the typical device photography, respectively. We measured the ρ_{xx} and SMR by using the devices shown in Figs. 5(c) and 5(d). For the measurements of SMR, the current, which is less than equal to 5 μA, is passed through the devices in the x-axis direction in Fig. 5(c) and external magnetic field between -4 and $+4$ T is applied in both y- and z-axis directions at 305 K.

Figure 5(e) shows the inverse of the device longitudinal resistance ($1/R_{xx}$) multiplied by a geometrical factor (L/w), the sheet conductance, $G_{xx} = L/(wR_{xx})$ values are plotted as a function of the total thickness of the HM layer (t_{total}) for typical devices of sample E and sample I. The lengths L and w are $L = 205$ μm and $w = 5.0$ μm as shown in Fig. 5(c). There is no anomaly in the G_{xx} vs t_{total} plot for the device for sample I, indicating no significant change in resistivity with increasing t_{total} as shown in Fig. 5(e). On the other hand, for the devices with Pt (sample E), the slope significantly increases in the thicker thickness region and there is anomaly at around $t_{total} = t_{Pt} \sim 3.5$ nm. This result indicates that the
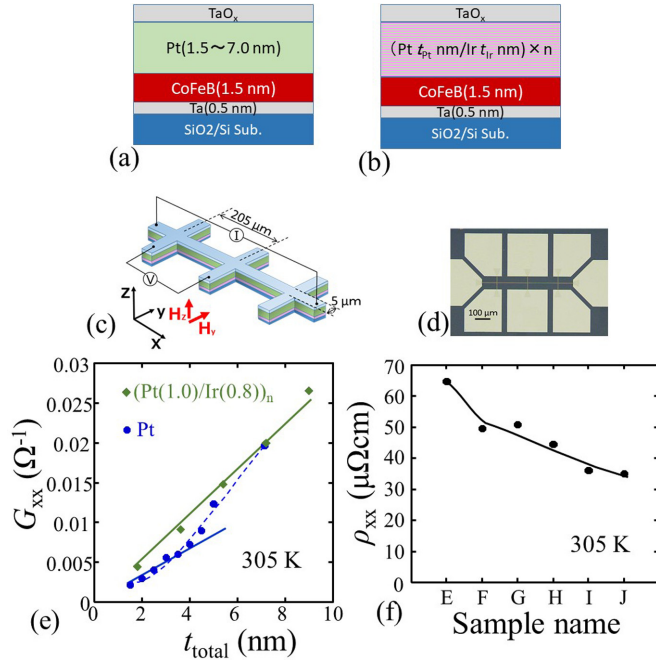
FIG. 5. (a), (b) Film stacks in prepared Hall bar devices. Schematic diagram of (c) prepared device and (d) photograph of the typical device. (e) Sheet conductance (G_{xx}) as a function of HM thickness (t_{total}). The solid lines in (e) are linear fits to the data and the dotted line in (e) is the least-square fit using Eq. (1). (f) Estimated resistivity (ρ_{xx}) for Pt, [Pt(0.4)/Ir(0.4)]$_n$, [Pt(0.6)/Ir(0.6)]$_n$, [Pt(0.8)/Ir(0.8)]$_n$, and [Pt(1.2)/Ir(0.8)]$_n$ HMs for samples E–J.

ρ_{xx} is large in the thin t_{Pt} region and becomes much smaller at the thicker t_{Pt} region. Solid lines in Fig. 5(e) are fitting results by least-squares method. For Pt, we used the data for the fitting in the region of $t_{total} = t_{Pt} \leqslant 3.5$ nm, because a recent report [56] shows that efficiency of SHE depends on the ρ_{xx} in the case of Pt HM. Since the slope of the solid lines in Fig. 5(e) is the inverse of the resistivity of HM ($1/\rho_{xx}$), we determined the ρ_{xx} values by fitting the slope of the solid lines of G_{xx} versus t_{total} plots as shown in Fig. 5(e). Figure 5(e) indicates that the resistivity ρ_{xx} value for [Pt(1.0)/Ir(0.8)]$_n$-multilayer HM is smaller than that for Pt in the region of $t_{total} \leqslant 7$ nm. Figure 5(f) shows resistivity ρ_{xx} values fitted by least-squares method for Pt and [Pt/Ir]$_n$-multilayer HMs. Thus, we found that the ρ_{xx} values in [Pt/Ir]$_n$-multilayer HMs are low compared to that in Pt. In the case of Pt layer, grain size increases with increasing t_{Pt}, leading to decrease of scattering by grain boundary. The dotted line in Fig. 5(e) shows the calculated resistivity of Pt, considering the scattering by both grain boundaries and film surfaces given by [57,58]

$$G_{xx} = \left[1 - \left(\frac{1}{2} + \frac{3}{4} \frac{\lambda_{mfp}}{t_{Pt}} \right) \left(1 - p \exp\left(-\frac{\zeta t_{Pt}}{\lambda_{mfp}} \right) \right) \right.$$
$$\left. \times \exp\left(-\frac{t_{Pt}}{\lambda_{mfp}} \right) \right] \Big/ \rho_\infty, \quad (1)$$

where the values $p = 1.0$ fraction of carriers secularly scattered at the surface of Pt layer, bulk resistivity $\rho_\infty = 9 \, \mu\Omega$ cm, mean-free path $\lambda_{mfp} = 26$ nm, and the grain-boundary penetration parameter $\zeta = 1.34$, using the resistivity value (ρ_{CoFeB})
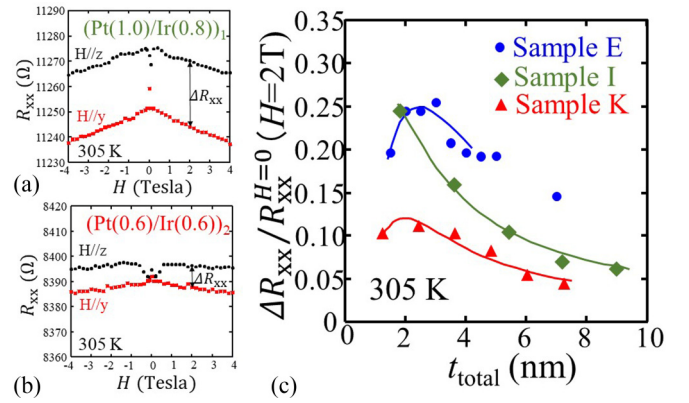

FIG. 6. Typical longitudinal resistance R_{xx} vs external magnetic field H oriented along the y axis (red squares) and z axis (black circles) measured at 305 K for the device with (a) [Pt(1.0)/Ir(0.8)]$_1$-multilayer HM and (b) [Pt(0.6)/Ir(0.6)]$_2$-multilayer HM. Typical SMR $\Delta R_{xx}/R_{xx}^{H=0}$ plotted against the HM layer thickness (t_{total}) for Pt and [Pt/Ir]-multilayer HM systems (samples E, I, and K). The solid lines show the fitting results using drift diffusion model.

for Co$_{20}$Fe$_{60}$B$_{20}$ is $\rho_{CoFeB} = 260.5 \, \mu\Omega$ cm, which is the obtained vertical intercept value by the fit shown in Fig. 5(e) (solid lines). As shown in Fig. 5(e), the experimental results can be well fitted by Eq. (1), indicating that anomaly in Pt system would be related to the scattering from grain boundaries [57,58]. As described in the part of Figs. 1(e) and 1(f), the cross-sectional HR-TEM results for sample E and sample I show smaller grain size of Pt than that of [Pt(1.0)/Ir(0.8)]$_2$-multilayer HM. These cross-sectional HR-TEM results are qualitatively consistent with the resistivity result shown in Fig. 5(e).

Figures 6(a) and 6(b) show the typical R_{xx} versus external magnetic field H for the devices for sample I ($n = 1$, $t_{total} = 1.8$ nm) and sample K ($n = 2$, $t_{total} = 2.4$ nm). Black closed circles and red closed squares are the R_{xx} data applying external magnetic field to $H//z$ and $H//y$ directions, respectively. Because the saturation field (H_s) measured by VSM is around $|H_s| = 1.5 \sim 2.0$ T, we plotted the magnitude of SMR ($\Delta R_{xx}/R_{xx}^{H=0}$) values at $H = 2$ T [$\Delta R_{xx}/R_{xx}^{H=0}(H = 2T)$] (average value of $\Delta R_{xx}/R_{xx}^{H=0}$ at $H = -2$ T and $+2$ T) as a function of t_{total} in Fig. 6(c). As shown in Fig. 6(c), the thickness t_{total} at which the maximum values of $\Delta R_{xx}/R_{xx}^{H=0}(H = 2T)$ in $\Delta R_{xx}/R_{xx}^{H=0}(H = 2T)$ vs t_{total} plot decrease with increasing inserting t_{Ir} in [Pt/Ir]-multilayer HM, which indicates the decrease in spin-diffusion length (λ_S) with increasing inserting t_{Ir}. The solid lines in Fig. 6(c) are the results fitted to the measured data by using the equations [54,55]

$$\text{SMR} = \Delta R_{xx}/R_{xx}^{H=0}(H = 2T)$$
$$\sim \theta_{SH}^2 \frac{\lambda_S}{t_{total}} \frac{\tanh(t_{total}/2\lambda_S)}{1 + \xi} \left[1 - \frac{1}{\cosh(t_{total}/\lambda_S)} \right], \quad (2)$$
$$\xi \equiv \frac{\rho_{HM} t_{CoFeB}}{\rho_{CoFeB} t_{total}}, \quad (3)$$

where $\rho_{CoFeB} = 260.5 \, \mu\Omega$ cm and ρ_{HM} are the resistivities of CoFeB and HM estimated by the least-square fitting shown in Fig. 5(d), respectively. As shown in Figs. 1(e) and 1(f), since
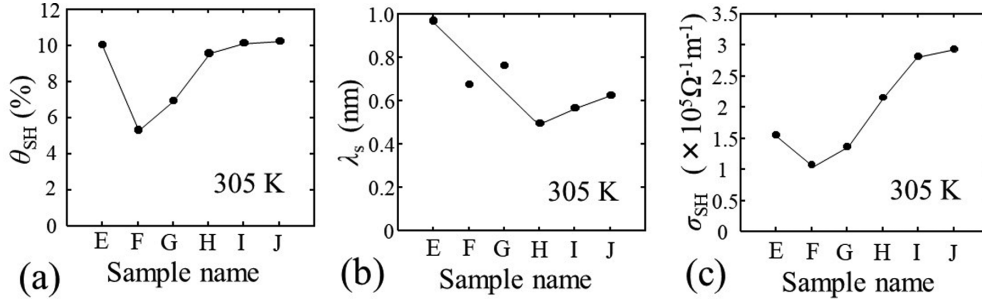
FIG. 7. (a) Estimated magnitude of the spin Hall angle (θ_{SH}), (b) spin-diffusion length (λ_S), and (c) spin Hall conductivity (σ_{SH}) for Pt and [Pt/Ir]-multilayer HM for samples E–J. The solid black lines in (a)–(c) are guides for the eyes.

the cross-sectional HR-TEM results show that the top Ta layer is fully oxidized, the SOT contribution from the top Ta layer is ignored in this evaluation. As shown in Fig. 6(c), the data are well fitted by using these equations (2) and (3).

Figures 7(a)–7(c) show the results of θ_{SH}, λ_S, and σ_{SH} obtained from the fit shown in Fig. 6(c). Figure 7(a) shows that the magnitude of θ_{SH} in [Pt(0.4)/Ir(0.4)]$_n$ HM is smaller than that of Pt and those in [Pt(1.0)/Ir(0.8)]$_n$ HM and [Pt(1.2)/Ir(0.8)]$_n$ HM are slightly larger than that in Pt. This result would indicate that SHE in [Pt/Ir]-multilayer HM is large compared to that of Pt, whereas SHE in [Pt/Ir]-multilayer HM with a large percentage of volume at the interface between Pt and Ir is small compared to that of Pt, because [Pt(0.4)/Ir(0.4)]$_n$ HM would have larger percentage of volume at the interface between Pt and Ir than those for [Pt(1.0)/Ir(0.8)]$_n$ HM and [Pt(1.2)/Ir(0.8)]$_n$ HM. The maximum magnitude of θ_{SH} is 10.3% for [Pt(1.2)/Ir(0.8)]$_n$ HM. Figure 7(b) shows that the magnitude of λ_S in [Pt/Ir]-multilayer HM is shorter than that in Pt. This would be related to the increase in the interfacial scattering of multilayer system. Figure 7(c) shows the plot of σ_{SH} for Pt and [Pt/Ir]$_n$-multilayer HMs. As shown in Fig. 7(c), the magnitude of σ_{SH} in [Pt(0.8)/Ir(0.8)]$_n$, [Pt(1.0)/Ir(0.8)]$_n$ and [Pt(1.2)/Ir(0.8)]$_n$-multilayer HMs is larger than that in Pt system. The σ_{SH} is defined as $\sigma_{SH} = |\sigma_{SH}|/\rho_{xx} = \sigma_{SH}^{int} - [\sigma_{SH}^{sj}\rho_{xx0}^2 + \alpha_{SS}\rho_{xx0}]/\rho_{xx}^2$, where the σ_{SH}^{int} is intrinsic spin Hall conductivity, σ_{SH}^{sj} is spin Hall conductivity due to the side-jump mechanism, α_{SS} is the skew scattering angle, and ρ_{xx0}

is the residual resistivity of heavy metal [41,42,59]. This equation and many experimental results [41–43,60] show that monotonous increase in $|\theta_{SH}|$ with increasing ρ_{xx} in relatively low ρ_{xx} region ($\rho_{xx} \leqslant 70 \mu\Omega$ cm). Therefore, large σ_{SH} indicates that HM has large $|\theta_{SH}|$ and low ρ_{xx}. This result is good from the application point of view.

Figures 8(a) and 8(b) show $\Delta R_{xx}/R_{xx}^{H=0}(H = 2$ T) (average value of $\Delta R_{xx}/R_{xx}^{H=0}$ at $H = -2$ T and $+2$ T) as a function of t_{total} for samples L–N and samples H–J. We investigated t_{Pt} dependence of ρ_{xx}, θ_{SH}, σ_{SH}, and λ_S for [Pt(t_{Pt})/Ir(t_{Ir})]$_n$-multilayer HM systems with $t_{Ir} = 0.6$ nm and $t_{Ir} = 0.8$ nm at which AF interlayer exchange coupling and F interlayer exchange coupling are observed, respectively (see Fig. 3). As shown in Figs. 8(a) and 8(b), monotonous increase of magnitude of $\Delta R_{xx}/R_{xx}^{H=0}(H = 2$ T) with increasing t_{Pt} was observed for both [Pt(t_{Pt})/Ir(0.6)]$_n$ and [Pt(t_{Pt})/Ir(0.8)]$_n$-multilayer HM systems. The solid lines in Figs. 8(a) and 8(b) are the results fitted to the measured data by using Eqs. (2) and (3). The data are well fitted by using these equations.

Figures 9(a)–9(d) show the t_{Pt} dependence of ρ_{xx}, θ_{SH}, σ_{SH}, and λ_S for [Pt(t_{Pt})/Ir(t_{Ir})]$_n$-multilayer HM systems with $t_{Ir} = 0.6$ nm and $t_{Ir} = 0.8$ nm (samples L–N and samples H–J). As shown in Figs. 9(a)–9(d), the t_{Pt} dependence of ρ_{xx}, θ_{SH}, σ_{SH}, and λ_S shows the same tendency between [Pt(t_{Pt})/Ir(t_{Ir})]$_n$-multilayer HM systems with $t_{Ir} = 0.6$ nm and $t_{Ir} = 0.8$ nm. As shown in Fig. 9(a), the magnitude of ρ_{xx} for both [Pt(t_{Pt})/Ir(t_{Ir})]$_n$-multilayer HM systems with $t_{Ir} = 0.6$ nm and $t_{Ir} = 0.8$ nm decreases with increasing t_{Pt}. All the magnitudes of θ_{SH}, σ_{SH}, and λ_S for both [Pt(t_{Pt})/Ir(t_{Ir})]$_n$-multilayer HM systems with $t_{Ir} = 0.6$ nm and $t_{Ir} = 0.8$ nm increase with increasing t_{Pt} as shown in Figs. 9(b)–9(d). The value of σ_{SH} of Pt HM is $1.56 \times 10^5 \Omega^{-1}$ m^{-1} as shown in Fig. 7(c). So, we observed large magnitude of σ_{SH} in [Pt(t_{Pt})/Ir(t_{Ir})]$_n$-multilayer HM systems compared to that in Pt as shown in Fig. 9(c). The observed value of θ_{SH} is 10.0% for Pt HM as shown in Fig. 7(a). Therefore, all the data values of θ_{SH} in [Pt(t_{Pt})/Ir(t_{Ir})]$_n$-multilayer HM systems shown in Fig. 9(b) are nearly the same with that for Pt. Therefore, large magnitude of σ_{SH} in [Pt(t_{Pt})/Ir(t_{Ir})]$_n$-multilayer HM systems is originating from the lower magnitude of ρ_{xx} in [Pt(t_{Pt})/Ir(t_{Ir})]$_n$-multilayer HM systems compared to that in Pt HM system. All values of θ_{SH} and σ_{SH} in [Pt(t_{Pt})/Ir(0.8)]$_n$-multilayer HM systems are larger than those in [Pt(t_{Pt})/Ir(0.6)]$_n$-multilayer HM systems. This indicates that the magnitudes of θ_{SH} and σ_{SH} increase with increasing t_{Ir} and that enhancement of SHE is related to the artificial multilayer structure. The length of all the λ_S
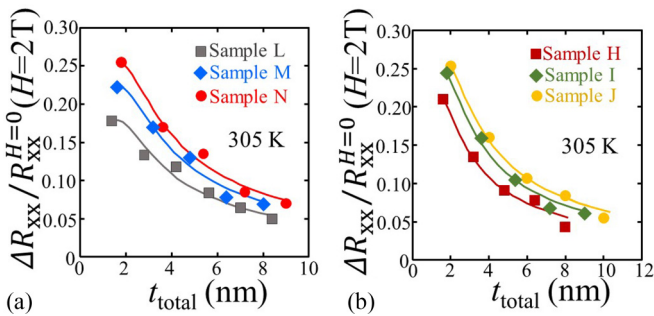

FIG. 8. SMR $\Delta R_{xx}/R_{xx}^{H=0}$ plotted against the HM layer thickness (t_{total}) for (a) samples L–N and (b) samples H–J with $t_{Pt} = 0.8$, 1.0, and 1.2 nm. The solid lines show the fitting results using drift diffusion model.

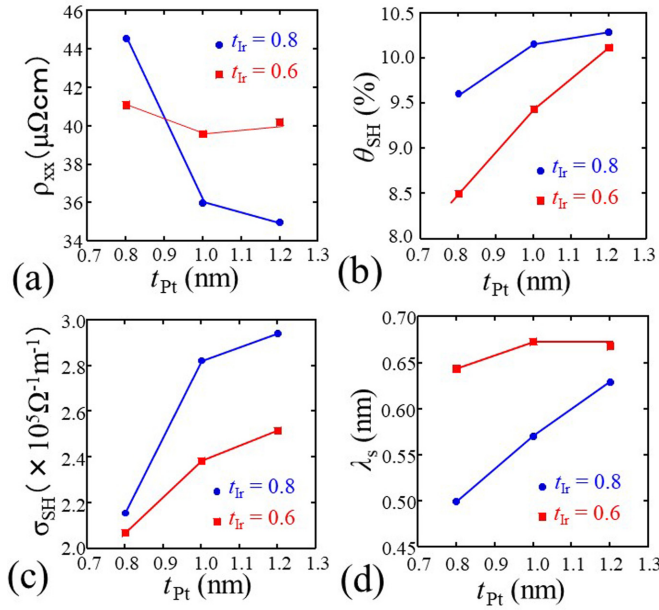FIG. 9. Pt thickness (t_{Pt}) dependence of (a) estimated magnitude of the resistivity (ρ_{xx}), (b) spin Hall angle (θ_{SH}), (c) spin Hall conductivity (σ_{SH}), and (d) spin-diffusion length (λ_S) for [Pt(t_{Pt})/Ir(0.6)] HMs (samples L–N) (red solid squares) and [Pt(t_{Pt})/Ir(0.8)] HMs (samples H–J) (blue solid circles). The solid red and blue lines in (a)–(d) are guides for the eyes.

in [Pt(t_{Pt})/Ir(t_{Ir})]$_n$-multilayer HM systems is shorter than that in Pt. This would be related to the increase in the interfacial scattering of multilayer system as discussed before. All values of λ_S in [Pt(t_{Pt})/Ir(0.8)]$_n$-multilayer HM systems ($t_{Ir} = 0.8$ nm) are shorter than those in [Pt(t_{Pt})/Ir(0.6)]$_n$-multilayer HM systems ($t_{Ir} = 0.6$ nm). This indicates that the interfacial scattering related to the artificial multilayer structure would be larger in [Pt(t_{Pt})/Ir(0.8)]$_n$-multilayer HM systems compared to that in [Pt(t_{Pt})/Ir(0.6)]$_n$-multilayer HM systems.

IV. DISCUSSION

First, let us discuss the reasons for the small magnitude of ρ_{xx} and short length of λ_S observed in [Pt(t_{Pt})/Ir(t_{Ir})]$_n$-multilayer HM systems compared to those in Pt system. One of the reasons why the magnitude of ρ_{xx} is small in [Pt(t_{Pt})/Ir(t_{Ir})]$_n$-multilayer HM system is related to that the grain size of [Pt(t_{Pt})/Ir(t_{Ir})]$_n$-multilayer HM system observed in the cross-sectional HR-TEM [Figs. 1(e) and 1(f)] is larger than that in Pt system as discussed before. Another reason for the small magnitude of ρ_{xx} would be related to having the same topology of Fermi surface between Pt and Ir. In Fig. 3, we observed the same AF oscillation period Λ in Co/Ir/Pt/Co system and Co/Pt/Co system. As discussed before, we also observed AF interlayer exchange coupling is maintained even through the thick Pt layer and monotonous decrease of magnitude of AF interlayer exchange coupling through t_{Pt} [see Fig. 4(c)]. This indicates that the spanning wave vector q_s in Fermi surface exists even through thick t_{Pt}; therefore, this would indicate that electrons could move freely to some extent at the Pt/Ir interface. This would be another reason for the small magnitude of ρ_{xx} in [Pt(t_{Pt})/Ir(t_{Ir})]$_n$-multilayer HM

system. On the other hand, as shown in Figs. 7(b) and 9(d), we observed short length of λ_S in [Pt(t_{Pt})/Ir(t_{Ir})]$_n$-multilayer HM systems compared to that in Pt system. These experimental results indicate that spins feel the difference between Pt and Ir; however, electrons do not feel the difference between Pt and Ir. Spins would feel the difference through the spin-orbit interaction due to the difference of the magnitude of orbital angular momentum between Pt and Ir.

Next, we would like to discuss the reason for the enhancement of efficiency of σ_{SH} observed in [Pt(t_{Pt})/Ir(t_{Ir})]$_n$-multilayer HM systems compared to that in Pt system. As described before, enhancements of θ_{SH} and σ_{SH} in [Pt(t_{Pt})/Ir(t_{Ir})]$_n$-multilayer HM systems could not be observed for the thin t_{Pt} and t_{Ir} as shown in Figs. 7(a) and 7(c). This indicates that the reason for the enhancements is not related to the scattering originating from the interface mixing phase of Pt-Ir but the scattering originating from the artificial multilayer system of Pt/Ir. Therefore, these results seem to indicate that the reason for the enhancements of θ_{SH} and σ_{SH} is correlated to that of decrease of the λ_S observed in [Pt(t_{Pt})/Ir(t_{Ir})]$_n$-multilayer HM systems. Spins would feel the difference of Pt and Ir through the spin-orbit interaction due to the difference of the magnitude of orbital angular momentum between Pt and Ir as described before. We think that there might exist a tradeoff between the magnitudes of θ_{SH} and λ_S. However, several previous papers [33,39,41–43,61,62] have suggested that the values of λ_S for Pt vary from 1 to 11 nm. The λ_S would be also related to the crystalline of the sample, spin memory loss at ferromagnet/HM interface [56], so, more experimental and theoretical efforts would be necessary for clarifying the absolute value of λ_S and the correlation between θ_{SH} and λ_S. Recently, there has been an interesting report [56] that the Elliott-Yafet scattering mechanism [63,64] provides the relation between θ_{SH} and λ_S.

From the application point of view, the discovery of the material with large magnitude of σ_{SH} (large $|\theta_{SH}|$ and low ρ_{xx}) is important. In this study, we observed the large magnitude of σ_{SH} in [Pt(t_{Pt})/Ir(t_{Ir})]$_n$-multilayer HM systems compared to that in Pt. The reasons for the enhancement of σ_{SH} observed in [Pt(t_{Pt})/Ir(t_{Ir})]$_n$-multilayer HM systems are related to the enhancement of $|\theta_{SH}|$ due to the scattering originating from the artificial multilayer system and decrease of ρ_{xx}, which would be originating from the same topology of Fermi surface between Pt and Ir. Thus, we could find a nonmagnetic spacer layer simultaneously exhibiting AF interlayer exchange coupling and having large $|\theta_{SH}|$, low ρ_{xx}, and the thickness sufficiently thicker than the spin-diffusion length. Since the Pt has already been utilized as a spin-current source for SOT switching [8,37], the observed synthetic AF coupling layer would be one of the promising systems for the systematic investigation of the SOT on the AF structure. Table II shows comparison of dampinglike SOT efficiency (θ_{SH}, $\xi_{DL} = T_{int} \theta_{SH}$), ρ_{xx}, and σ_{SH} for various nonmagnetic metals which reported as nonmagnetic spacer of synthetic AF structure and for recently reported various heavy metals having Pt-based alloys [65–68], where $T_{int} (< 1)$ is the interfacial spin transparency. As shown in Table II, the Pt alloys result in much improved SOT efficiency. Because these Pt alloys have a fcc structure, the same structure of Ir and Pt alloys (such as $Pt_{0.75}Au_{0.25}$, $Pt_{0.75}Pd_{0.25}$, $Pt_{0.57}Cu_{0.43}$, $Pt_{0.85}Hf_{0.15}$,

TABLE II. Comparison of dampinglike SOT efficiency (θ_{SH}, ξ_{DL}), ρ_{xx}, and σ_{SH} for various nonmagnetic metals reported as nonmagnetic spacer of synthetic AF structure, and for various heavy metals having Pt-based alloys.

Heavy metals	θ_{SH}, ξ_{DL} (%)	ρ_{xx} [$\mu\Omega$ cm]	σ_{SH} ($10^5 \hbar/2e\Omega^{-1}$ m^{-1})	AF coupling	Ref.
Pt/Ir/Pt, (Pt/Ir)$_n$	8.5~10.3	35~41	2.1~2.95	Yes	This work
Cu$_{95}$Ir$_5$	3~4	92.4	0.3~0.43	Yes	[16]
Ru	0.6	No data	No data	Yes	[38]
Ir	2	25	0.8	Yes	[39]
Cu	0.3	6.3	0.48	Yes	[40]
Pt (3.5 nm)	10	64.8	1.56	No	This work
Pt	6~10	24.5~40	2~3.1	No	[33,39,41–43]
Pt$_{0.75}$Au$_{0.25}$	30	83	3.6	No data	[65]
Pt$_{0.75}$Pd$_{0.25}$	26	57.5	4.5	No data	[66]
Pt$_{0.57}$Cu$_{0.43}$	44	82.5	5.3	No data	[67]
Pt$_{0.85}$Hf$_{0.15}$	16	110	1.45	No data	[68]
Pt$_{0.8}$Al$_{0.2}$	14	75	1.87	No data	[68]

and Pt$_{0.8}$Al$_{0.2}$) suggests that topological characteristic of the Fermi surface of Ir and Pt alloys are nearly the same, which would be closely related to the q_s linking two points of Fermi surface with antiparallel velocities in the case of noble-metal spacer [46,47]. Therefore, if the technology we proposed in this study and Pt alloy technology can be fused, the fusion technology of Co/Pt alloy/Ir/Pt alloy/Co synthetic AF coupling layer structure (Pt alloys: Pt$_{0.75}$Au$_{0.25}$, Pt$_{0.75}$Pd$_{0.25}$, Pt$_{0.57}$Cu$_{0.43}$, Pt$_{0.85}$Hf$_{0.15}$, and Pt$_{0.8}$Al$_{0.2}$) might be an excellent candidate simultaneously exhibiting AF interlayer exchange coupling and huge SHE. Further experimental efforts in the synthetic AF coupling layer would be necessary.

Finally, we would like to discuss the possibility of the further increase of σ_{SH} in the synthetic AF coupling layer structure of ferromagnet/Pt/Ir/Pt/ferromagnet structure by using another approach. As shown in Figs. 9(b) and 9(c), we could not observe the enhancements of σ_{SH} and $|\theta_{SH}|$ in the ferromagnet/[Pt(t_{Pt})/Ir(t_{Ir})]$_n$ HM system with one ferromagnetic layer and with t_{Ir} in which AF coupling has been observed compared to those with F coupling. This result is consistent with the previous result [16] which studied the SHE using ferromagnet/Cu$_{95}$Ir$_5$ alloy HM system with one ferromagnetic layer. In synthetic AF coupling layer with completely compensated magnetization, evaluation of the efficiency of SHE is difficult and determination of SOT efficiencies in synthetic AF remains elusive [69,70]. More recently reported papers show enhancement of SHE in synthetic AF coupling system [49,71]. One of them [71] using Pt located outside the synthetic AF coupling layer for evaluation of SOT efficiency and another paper [49] evaluates the SOT efficiency using synthetic AF coupling layer with uncompensated magnetization with three ferromagnetic layers. Model calculations based on the Landau-Lifshitz-Gilbert equation [49] show that the presence of antiferromagnetic coupling can increase the SOT due to the existence of the exchange coupling field (H_{ex}) defined in Fig. 2. However, the model could not explain the experimentally observed magnitude of the SHE enhancement in synthetic AF coupling layer [49]. They conclude that there are other sources of SOT besides H_{ex} that may account for the highly efficient SOT acting on synthetic AF coupling layer. Particularly, for the ferromag-

net/Pt/Ir/Pt/ferromagnet system we proposed in this study, the efficiency of SHE changes depending on the film thicknesses of Pt and Ir as shown in Figs. 7(a), 7(c), 9(b), and 9(c); therefore, it is expected that the result of the SOT efficiency in the ferromagnet/Pt/Ir/Pt/ferromagnet system will show more complex result. Further experimental and theoretical efforts in the synthetic AF coupling layer with completely compensated and uncompensated magnetization, and/or with various magnitude of exchange coupling strength, and/or with in-plane and out-of-plane magnetization, are required to clarify the origin of the SOT in synthetic AF coupling layer.

V. SUMMARY

We have investigated the interlayer exchange coupling in Co/nonmagnetic spacer layer/Co systems with multilayer structure of Pt/Ir and Pt/Ir/Pt for the nonmagnetic spacer layer, and compared to that with Ir nonmagnetic spacer layer. The AF interlayer exchange coupling was observed even for the Pt/Ir/Pt nonmagnetic spacer layer samples. The AF interlayer exchange coupling in the wide range of Pt thickness ($0 \leqslant t_{Pt} \leqslant 1.0$ nm) and in the wide range of total thickness of nonmagnetic spacer layer ($1.0 \leqslant t_{total} \leqslant 2.5$ nm) was also observed. Moreover, we have evaluated the SHE for Pt/Ir multilayer systems, and observed the enhancement of spin Hall conductivity and spin Hall angle compared to those in Pt system. This study has clarified that Pt/Ir/Pt is a promising nonmagnetic spacer layer simultaneously exhibiting AF interlayer exchange coupling and having large $|\theta_{SH}|$, low ρ_{xx}, and the thickness sufficiently thicker than the spin-diffusion length. We expect the Pt/Ir/Pt spacer layer to pave a way to the antiferromagnetic spintronics based on the multilayer systems.

[1] T. Jungwirth, X. Marti, P. Wadley, and J. Wunderlich, Nat. Nanotechnol. **11**, 231 (2016).

[2] V. Baltz, A. Manchon, M. Tsoi, T. Moriyama, T. Ono, and Y. Tserkovnyak, Rev. Mod. Phys. **90**, 015005 (2018).

[3] Z. Wei, A. Sharma, A. S. Nunez, P. M. Haney, R. A. Duine, J. Bass, A. H. MacDonald, and M. Tsoi, Phys. Rev. Lett. **98**, 116603 (2007).

[4] L. Néel, http://www.nobelprize.org/nobel_prizes/physics/laureates/1970/neel-lecture.pdf.

[5] D. Houssameddine, J. F. Sierra, D. Gusakova, B. Delaet, U. Ebels, L. D. Buda-Prejbeanu, M. C. Cyrille, B. Dieny, B. Ocker, J. Langer, and W. Maas, Appl. Phys. Lett. **96**, 072511 (2010).

[6] K. Tanaka, T. Moriyama, M. Nagata, T. Seki, K. Takanashi, S. Takahashi, and T. Ono, Appl. Phys. Exp. **7**, 063010 (2014).

[7] P. Wadley, B. Howells, J. Železný, C. Andrews, V. Hills, R. P. Campion, V. Novák, K. Olejník, F. Maccherozzi, S. S. Dhesi, S. Y. Martin, T. Wagner, J. Wunderlich, F. Freimuth, Y. Mokrousov, J. Kuneš, J. S. Chauhan, M. J. Grzybowski, A. W. Rushforth, K. Edmond *et al.*, Science **351**, 587 (2016).

[8] T. Moriyama, K. Oda, T. Ohkochi, M. Kimata, and T. Ono, Sci. Rep. **8**, 14167 (2018).

[9] S. Y. Bodnar, L. Šmejkal, I. Turek, T. Jungwirth, O. Gomonay, J. Sinova, A. A. Sapozhnik, H. J. Elmers, M. Kläui, and M. Jourdan, Nat. Commun. **9**, 348 (2018).

[10] T. Moriyama, W. Zhou, T. Seki, K. Takanashi, and T. Ono, Phys. Rev. Lett. **121**, 167202 (2018).

[11] X. Z. Chen, R. Zarzuela, J. Zhang, C. Song, X. F. Zhou, G. Y. Shi, F. Li, H. A. Zhou, W. J. Jiang, F. Pan, and Y. Tserkovnyak, Phys. Rev. Lett. **120**, 207204 (2018).

[12] W. Zhou, T. Seki, T. Kubota, G. E. W. Bauer, and K. Takanashi, Phys. Rev. Mater. **2**, 094404 (2018).

[13] M. Meinert, D. Graulich, and T. Matalla-Wagner, Phys. Rev. Appl. **9**, 064040 (2018).

[14] M. J. Grzybowski, P. Wadley, K. W. Edmonds, R. Beardsley, V. Hills, R. P. Campion, B. L. Gallagher, J. S. Chauhan, V. Novak, T. Jungwirth, F. Maccherozzi, and S. S. Dhesi, Phys. Rev. Lett. **118**, 057701 (2017).

[15] A. A. Sapozhnik, M. Filianina, S. Y. Bodnar, A. Lamirand, M. A. Mawass, Y. Skourski, H. J. Elmers, H. Zabel, M. Kläui, and M. Jourdan, Phys. Rev. B **97**, 134429 (2018).

[16] H. Masuda, T. Seki, Y.-C. Lau, T. Kubota, and K. Takanashi, Phys. Rev. B **101**, 224413 (2020).

[17] L. Liu, C.-F. Pai, Y. Li, H. W. Tseng, D. C. Ralph, and R. A. Buhrman, Science **336**, 555 (2012).

[18] G. Yu, P. Upadhyaya, Y. Fan, J. G. Alzate, W. Jiang, K. L. Wong, S. Takei, S. A. Bender, L.-T. Chang, Y. Jiang, M. Lang, J. Tang, Y. Wang, Y. Tserkovnyak, P. K. Amiri, and K. L. Wang, Nat. Nanotechnol. **9**, 548 (2014).

[19] W. Jiang, P. Upadhyaya, W. Zhang, G. Yu, M. B. Jungfleisch, F. Y. Fradin, J. E. Pearson, Y. Tserkovnyak, K. L. Wang, O. Heinonen, S. G. E. Velthuis, and A. Hoffmann, Science **349**, 283 (2015).

[20] P. P. J. Haazen, E. Mure, J. H. Franken, R. Lavrijsen, H. J. M. Swagten, and B. Koopmans, Nat. Mater. **12**, 299 (2013).

[21] A. Chernyshov, M. Overby, X. Liu, J. K. Furdyna, Y. Lyanda-Geller, and L. P. Rokhinson, Nat. Phys. **5**, 656 (2009).

[22] I. M. Miron, K. Garello, G. Gaudin, P.-J. Zermatten, M. V. Costache, S. Auffret, S. Bandiera, B. Rodmacq, A. Schuhl, and P. Gambardella, Nature (London) **476**, 189 (2011).

[23] J. Kim, J. Sinha, M. Hayashi, M. Yamanouchi, S. Fukami, T. Suzuki, S. Mitani, and H. Ohno, Nat. Mater. **12**, 240 (2013).

[24] S. Fukami, T. Anekawa, C. Zhang, and H. Ohno, Nat. Nanotechnol. **11**, 621 (2016).

[25] K.-S. Lee, S.-W. Lee, B.-C. Min, and K.-J. Lee, Appl. Phys. Lett. **104**, 072413 (2014).

[26] K. Garello, C. O. Avci, I. M. Miron, M. Baumgartner, A. Ghosh, S. Auffret, O. Boulle, G. Gaudin, and P. Gambardella, Appl. Phys. Lett. **105**, 212402 (2014).

[27] C. Zhang, S. Fukami, H. Sato, F. Matsukura, and H. Ohno, Appl. Phys. Lett. **107**, 012401 (2015).

[28] M.-H. Nguyen, C.-F. Pai, K. X. Nguyen, D. A. Muller, D. C. Ralph, and R. A. Buhrman, Appl. Phys. Lett. **106**, 222402 (2015).

[29] S. V. Aradhya, G. E. Rowlands, J. Oh, D. C. Ralph, and R. A. Buhrman, Nano Lett. **16**, 5987 (2016).

[30] M. Baumgartner, K. Garello, J. Mendil, C. O. Avci, E. Grimaldi, C. Murer, J. Feng, M. Gabureac, C. Stamm, Y. Acremann, S. Finizio, S. Wintz, J. Raabe, and P. Gambardella, Nat. Nanotechnol. **12**, 980 (2017).

[31] Y. Kato, Y. Saito, H. Yoda, T. Inokuchi, S. Shirotori, N. Shimomura, S. Oikawa, A. Tiwari, M. Ishikawa, M. Shimizu, B. Altansargai, H. Sugiyama, K. Koi, Y. Ohsawa, and A. Kurobe, Phys. Rev. Appl. **10**, 044011 (2018).

[32] Y. Saito, N. Tezuka, S. Ikeda, H. Sato, and T. Endoh, Appl. Phys. Exp. **12**, 053008 (2019).

[33] Y. Saito, N. Tezuka, S. Ikeda, H. Sato, and T. Endoh, AIP. Adv. **9**, 125312 (2019).

[34] Y. Saito, N. Tezuka, S. Ikeda, H. Sato, and T. Endoh, Appl. Phys. Lett. **116**, 132401 (2020).

[35] P. Grünberg, R. Schreiber, Y. Pang, M. B. Brodsky, and H. Sowers, Phys. Rev. Lett. **57**, 2442 (1986).

[36] C. Carbone and S. F. Alvarado, Phys. Rev. B **36**, 2433(R) (1987).

[37] Z. Dai, W. Liu, X. Zhao, L. Liu, and Z. Zhang, ACS Appl. Electron. Mater. **3**, 611 (2021).

[38] Z. Wen, J. Kim, H. Sukegawa, M. Hayashi, and S. Mitani, AIP Adv. **6**, 056307 (2016).

[39] T. Fache, J. C. Rojas-Sanchez, L. Badie, S. Mangin, and S. Petit-Watelot, Phys Rev B **102**, 064425 (2020).

[40] H. L. Wang, C. H. Du, Y. Pu, R. Adur, P. C. Hammel, and F. Y. Yang, Phys Rev. Lett. **112**, 197201 (2014).

[41] R. Ramaswamy, Y. Wang, M. Elyasi, M. Motapothula, T. Venkatesan, X. Qiu, and H. Yang, Phys Rev. Appl. **8**, 024034 (2017).

[42] M. Isasa, E. Villamor, L. E. Hueso, M. Gradhand, and F. Casanova, Phys Rev B **91**, 024402 (2015).

[43] L. Wang, R. J. H. Wesselink, Y. Liu, Z. Yuan, K. Xia, and P. J. Kelly, Phys. Rev. Lett. **116**, 196602 (2016).

[44] Y. Saito, N. Tezuka, S. Ikeda, H. Sato, and T. Endoh, AIP. Adv. **11**, 025007 (2021).

[45] K. Yakushiji, A. Sugihara, A. Fukushima, H. Kubota, and S. Yuasa, Appl. Phys. Lett. **110**, 092406 (2017).

[46] P. Bruno and C. Chappert, Phys. Rev. Lett. **67**, 1602 (1991).

[47] P. Bruno, J. Phys.: Condens. Matter **11**, 9403 (1999).

[48] K. W. Shin, S. Song, H.-W. Kim, G.-D. Lee, and E. Yoon, Jpn. J. Appl. Phys. **57**, 065504 (2018).

[49] Y. Ishikuro, M. Kawaguchi, T. Taniguchi, and M. Hayashi, Phys. Rev. B **101**, 014404 (2020).

[50] P. J. H. Bloemen, H. W. van Kesteren, H. J. M. Swagten, and W. J. M. de Jonge, Phys. Rev. B **50**, 13505 (1994).

[51] W. Folkerts, J. Magn. Magn. Mater. **94**, 302 (1991).

[52] M. Kawaguchi, D. Towa, Y. C. Lau, S. Takahashi, and M. Hayashi, Appl. Phys. Lett. **112**, 202405 (2018).

[53] H. Nakayama, M. Althammer, Y.-T. Chen, K. Uchida, Y. Kajiwara, D. Kikuchi, T. Ohtani, S. Geprägs, M. Opel, S. Takahashi, R. Gross, G. E. W. Bauer, S. T. B. Goennenwein, and E. Saitoh, Phys. Rev. Lett. **110**, 206601 (2013).

[54] J. Liu, T. Ohkubo, S. Mitani, K. Hono, and M. Hayashi, Appl. Phys. Lett. **107**, 232408 (2015).

[55] J. Kim, P. Sheng, S. Takahashi, S. Mitani, and M. Hayashi, Phys. Rev. Lett. **116**, 097201 (2016).

[56] M.-H. Nguyen, D. C. Ralph, and R. A. Buhrman, Phys. Rev. Lett. **116**, 126601 (2016).

[57] P. Fan, K. Yi, J.-D. Shao, and A.-X. Fan, J. Appl. Phys. **95**, 2527 (2004).

[58] S. Dushenko, M. Hokazono, K. Nakamura, Y. Ando, T. Shinjo, and M. Shiraishi, Nat. Commun. **9**, 3118 (2018).

[59] A. Kumar, R. Bansal, S. Chaudhary, and P. K. Muduli, Phys. Rev. B **98**, 104403 (2018).

[60] C. Zhang, S. Fukami, K. Watanabe, A. Ohkawara, S. DuttaGupta, H. Sato, F. Matsukura, and H. Ohno, Appl. Phys. Lett. **109**, 192405 (2016).

[61] J.-C. Rojas-Sánchez, N. Reyren, P. Laczkowski, W. Savero, J.-P. Attané, C. Deranlot, M. Jamet, J.-M. George, L. Vila, and H. Jaffrès, Phys. Rev. Lett. **112**, 106602 (2014).

[62] C. Stamm, C. Murer, M. Berritta, J. Feng, M. Gabureac, P. M. Oppeneer, and P. Gambardella, Phys. Rev. Lett. **119**, 087203 (2017).

[63] R. J. Elliott, Phys. Rev. **96**, 266 (1954).

[64] Y. Yafet, Solid State Phys. **14**, 1 (1963).

[65] L. Zhu, D. C. Ralph, and R. A. Buhrman, Phys. Rev. Appl. **10**, 031001(R) (2018).

[66] L. Zhu, K. Sobotkiewich, X. Ma, X. Li, D. C. Ralph, and R. A. Buhrman, Adv. Funct. Mater. **29**, 1805822 (2019).

[67] C.-Y. Hu and C.-F. Pai, Adv. Quantum Technol. **3**, 2000024 (2020).

[68] M.-H. Nguyen, M. Zhao, D. C. Ralph, and R. A. Buhrman, Appl. Phys. Lett. **108**, 242407 (2016).

[69] C. Bi, H. Almasi, K. Price, T. Newhouse-Illige, M. Xu, S. R. Allen, X. Fan, and W. Wang, Phys. Rev. B **95**, 104434 (2017).

[70] G. Y. Shi, C. H. Wan, Y. S. Chang, F. Li, X. J. Zhou, P. X. Zhang, J. W. Cai, X. F. Han, F. Pan, and C. Song, Phys. Rev. B **95**, 104435 (2017).

[71] P. X. Zhang, L. Y. Liao, G. Y. Shi, R. Q. Zhang, H. Q. Wu, Y. Y. Wang, F. Pan, and C. Song, Phys. Rev. B **97**, 214403 (2018).

[72] Y. Yafet, Phys. Rev. B **36**, 3948 (1987).

[73] W. Baltensperger and J. S. Helman, Appl. Phys. Lett. **57**, 2954 (1990).